

***Ab initio* charge transfer multiplet calculations on the $L_{2,3}$ XANES and ELNES of $3d$ transition metal oxides**

Hidekazu Ikeno,^{1,*} Teruyasu Mizoguchi,² and Isao Tanaka³¹*Fukui Institute for Fundamental Chemistry, Kyoto University, Takano-Nishihiraki, Sakyo, Kyoto 606-8103, Japan*²*Institute of Industrial Science, The University of Tokyo, 4-6-1, Komaba, Meguro, Tokyo 153-8505, Japan*³*Department of Materials Science and Engineering, Kyoto University, Yoshida, Sakyo, Kyoto 606-8501, Japan*

(Received 13 January 2011; revised manuscript received 21 February 2011; published 11 April 2011)

The $L_{2,3}$ x-ray absorption near-edge structures (XANES) and electron energy loss near-edge structures (ELNES) of $3d$ transition metal (TM) oxides are systematically calculated by the *ab initio* charge transfer multiplet (CTM) method using fully relativistic molecular spinors on the basis of density-functional theory. The electronic excitation from molecular spinors mainly composed of O- $2p$ to those of TM- $3d$, that is, charge transfer, is included by considering additional electronic configurations in the configuration interactions. The effects of the covalency and charge transfer on the TM- $L_{2,3}$ XANES are investigated in detail. The power of the *ab initio* CTM method to quantitatively reproduce the spectra is demonstrated. Meanwhile, limitations of the application of the method are discussed.

DOI: [10.1103/PhysRevB.83.155107](https://doi.org/10.1103/PhysRevB.83.155107)

PACS number(s): 78.70.Dm, 31.15.am, 71.15.Qe

I. INTRODUCTION

Both x-ray absorption near-edge structures (XANES) and electron energy loss near-edge structures (ELNES) are powerful techniques to observe the electronic structure of selected elements in materials.^{1,2} They monitor the electronic transition from core states to unoccupied states. Thus, they reflect information about the oxidation states, spin states, chemical bonding, and atomic coordinates of the element of interest.^{3,4} XANES is particularly useful for examining trace amounts of elements. ELNES can be used for sub-nanometer-scale analysis. Their application is not limited to crystals and they can be applied to amorphous and lattice imperfections. To extract such information, however, a good theoretical tool that has predictive performance without using adjustable parameters is indispensable.

Two approaches have been used to compute XANES/ELNES theoretically within the independent particle approximation. One is called the multiple-scattering approach, which basically computes the scattering phenomena of the excited electron associated with x-ray absorption or electron energy loss.⁵⁻⁷ This approach is also a standard technique for analyzing extended x-ray absorption fine structures (EXAFS). The other approach is a density-functional calculation using a large supercell with the inclusion of a core hole.⁸⁻¹⁰ Most of the K XANES/ELNES and $L_{2,3}$ XANES/ELNES of typical elements can be well reproduced by the independent particle approximation.

In the case of $3d$ transition metal (TM) $L_{2,3}$ XANES/ELNES, which are dominated by the $2p$ - $3d$ transition, the independent particle approximation breaks down. Spectra show widely spread multiplet structures because of the strong electronic correlations among spatially localized $2p$ core-hole and $3d$ electrons. To treat the electronic transition from the core level, relativistic effects should also be considered. In many $3d$ TM compounds, neighboring ligand atoms contribute to the spectral shapes of $L_{2,3}$ XANES/ELNES. In the case of $3d$ TM oxides, strong covalent bonding exists between the TM- $3d$ and the O- $2p$ states. In addition, the

charge transfer (CT) from oxygen ions to TM ions plays an important role in determining the spectral shapes of the TM- $L_{2,3}$ XANES/ELNES of some $3d$ TM oxides. Thus, the contribution of ligand ions should be included in the calculation of TM- $L_{2,3}$ XANES/ELNES.

Conventional theoretical approaches for the analysis of TM $L_{2,3}$ XANES/ELNES have been the semiempirical ligand field multiplet (LFM) method and the charge transfer (CT) multiplet (CTM) method, where crystal field effects are incorporated into an atomic multiplet calculation using the group theoretical formalism.¹¹⁻¹⁴ In both the LFM and the CTM approaches, the ligand field effects are considered using empirical parameters. In the CTM approach, the contribution of ligand orbitals is treated as the configuration interaction (CI) with an additional atomic configuration, that is., $3d^n + 3d^{n+1}\underline{L}$ for the initial state and $2p^5 3d^{n+1} + 2p^5 3d^{n+2}\underline{L}$ for the final states, where \underline{L} denotes a hole on ligand orbitals. CT energy and hopping integrals between the ligand state and $3d$ are introduced as additional empirical parameters to describe energy levels. Sometimes two or more charge-transferred configurations are considered. The agreement between experiments and theory is improved for covalent systems or high-valency systems by including the charge-transferred configurations. However, this method has a clear limitation because of the use of adjustable parameters. The number of parameters increases when the TM ion is located in lower symmetry sites, which decreases the predictive performance of multiplet structures.

Recently, several nonempirical approaches to TM- $L_{2,3}$ XANES/ELNES have been developed. The present authors have developed a relativistic CI method for XANES/ELNES using a small cluster model. The four-component wave functions, which are the eigensolutions of a single-particle Dirac equation, are used as the basis for a CI calculation. In this paper, the four-component single-particle wave function is referred to as a “spinor” in the strict sense. The interactions among a $2p$ core-hole and $3d$ electrons are rigorously taken into account. All ligand field effects are included by using molecular spinors instead of atomic spinors. Experimental spectra from many compounds with different d -electron

numbers and coordination numbers have been successfully reproduced without any empirical parameters.^{15–18} The CT from ligands to TM spinors can be included by considering additional electronic configurations in the CI.^{19,20} In this paper, we refer to this approach as the *ab initio* CTM approach, in contrast to the semiempirical CTM approach, as both of them are based on CI theory.

Krüger and Natoli developed the multichannel multiple-scattering (MCMS) theory.²¹ In the MCMS approach, the multiplet effects of $2p^5$ and the excited electron at final states are rigorously taken into account by the CI scheme. The interaction with the other electrons was taken into account through the effective one-electron potential optimized for the system. The MCMS method can handle larger cluster models including several hundred atoms and, thus, can virtually include solid-state effects. The TM- $L_{2,3}$ XANES of several d^0 compounds, that is, CaO, CaF₂, SrTiO₃, and TiO₂,^{22,23} have been successfully reproduced.

The band structure calculation based on the Bethe-Salpeter equation (BSE) has also been applied to the TM- $L_{2,3}$ XANES. In the BSE approach, the two-particle equation for a core hole and an excited electron, namely, a core exciton, is solved. Shirley developed a BSE method on top of the plane-wave-based pseudopotential method and calculated the TM- $L_{2,3}$ XANES of SrTiO₃, TiO₂, and CaF₂.²⁴ Very recently, Laskowski and Blaha implemented an all-electron relativistic BSE method on top of the augmented plane-wave plus local orbital (APW + *lo*) method (WIEN2k code). The Ti- $L_{2,3}$ XANES of d^0 compounds, as described above, have been reproduced well.²⁵ In both cases, the solid-state effects are *de facto* included. At the moment, however, the BSE method and the MCMS method have only been applied successfully for d^0 systems.

In this paper, we focus on the *ab initio* CTM method, which can describe the full multiplet structures among $2p$ and $3d$ electrons. TM- $L_{2,3}$ XANES spectra for $3d$ TM oxides with various d -electron numbers and symmetries are systematically calculated by this approach. The CT from oxygen to TM elements is explicitly considered by including the electronic configurations with a ligand hole in the CI. In Sec. II, the *ab initio* CTM approach is briefly introduced. In Sec. III, the effect of the covalent bonding between TM- $3d$ and O- $2p$ atomic spinors on the Coulomb interaction and multiplet structures is discussed. Then the effects of the CT on the spectral shape are described. In Sec. IV, the limitations to the current *ab initio* CTM approach are described.

II. COMPUTATIONAL PROCEDURE

A. Theory

The effective many-electron Hamiltonian adopted in the present work is the “no-pair” Hamiltonian,^{26,27} which is described in the second quantized form in atomic units as

$$\hat{H} = \sum_{i,j=1}^L \langle i|\hat{h}|j\rangle a_i^\dagger a_j + \frac{1}{2} \sum_{i,j,k,l=1}^L \langle ij|r_{12}^{-1}|kl\rangle a_i^\dagger a_j^\dagger a_l a_k, \quad (1)$$

where i , j , k , and l indicate molecular spinors, N is the number of electrons in the system, and $L > N$ is the number of given molecular spinors. a_i^\dagger and a_i denote the creation

and annihilation operators for an electron in the i th spinor, respectively. $\langle i|\hat{h}|j\rangle$ and $\langle ij|r_{12}^{-1}|kl\rangle$ are the one-electron and two-electron integrals over the four-component molecular spinors, respectively.

In the present work, a hybrid method of density-functional theory and CI (DFT-CI) is used. In the DFT-CI approach, electronic correlations among particularly important spinors, that is, molecular spinors mainly composed of TM- $2p$, $3d$, and O- $2p$ atomic spinors, are taken into account in the CI scheme, while the electronic correlations among the other electrons are treated within the framework of DFT. Thus, the single-particle operator \hat{h} is expressed as

$$\hat{h} = c\boldsymbol{\alpha} \cdot \mathbf{p} + mc^2\beta + v_{\text{ext}} + U'_{\text{DFT}}, \quad (2)$$

where v_{ext} is the electrostatic potential from nuclei plus other external potentials. Here U'_{DFT} denotes the Coulomb and the approximated exchange-correlation potential from electrons that are not explicitly considered in the CI calculation.

The many-electron wave function is expressed as a linear combination of Slater determinants, that is,

$$|\Psi_k\rangle = \sum_p C_{pk} |\Phi_p\rangle, \quad (3)$$

where $|\Phi_p\rangle = a_{p_1}^\dagger \cdots a_{p_N}^\dagger |\text{vac}\rangle$ is a Slater determinant constructed from the p_1, \dots, p_N th molecular spinors, and $|\text{vac}\rangle$ denotes the vacuum state. The coefficients C_{pk} in Eq. (3) and the corresponding eigenvalue E_k are determined by solving a standard Hermitian eigenvalue problem for the Hamiltonian matrix H , whose matrix elements are given as $\langle \Phi_p | \hat{H} | \Phi_q \rangle$.

The Hamiltonian matrix is fully diagonalized to obtain possible initial and final states. Then the oscillator strength of the electric dipole transition is evaluated as

$$I_{if} = \frac{2m}{\hbar^2} (E_f - E_i) \left| \left\langle \Psi_f \left| \sum_{k=1}^N \boldsymbol{\epsilon} \cdot \mathbf{r}_k \right| \Psi_i \right\rangle \right|^2, \quad (4)$$

where Ψ_i and Ψ_f are the many-electron wave functions for the initial and final states, while E_i and E_f are their energies, respectively. The photoabsorption cross section (PACS) was obtained by broadening the oscillator strengths using Lorentz functions and by multiplying by the constant $2\pi^2 \hbar^2 \alpha / m$. The full width at half-maximum (FWHM) of the Lorentz function was set to 0.6 eV over the whole energy region. In the case of $3d$ TM- $L_{2,3}$ XANES/ELNES, the quadrupole and higher order transitions are at least two orders of magnitude weaker than the dipole transitions and can be neglected. More details on the method are described in Ref. 19.

This CI method is known to systematically overestimate the absolute transition energy. This can be ascribed to the truncation of the Slater determinants. In other words, this is due to disregarding the minor contribution of the electronic correlations. In the present study, the transition energy was corrected by taking the energy difference between single-electron spinors for the Slater’s transition state as a reference.¹⁵

B. Relativistic molecular spinor calculations

Relativistic molecular spinor calculations were carried out by solving Dirac equations employing the local density approximation (LDA) using an in-house code. Four-component

relativistic molecular spinors were expressed as linear combinations of atomic spinors. The numerically generated four-component relativistic atomic spinors ($1s-4p$ for TM and $1s-2p$ for O) were used as basis functions for molecular spinors. Cluster models composed of one TM ion and the coordinating oxygen ions were used for the calculation. The total number of electrons in the cluster was counted on the basis of the formal charges of the constituents. The atomic positions of crystalline compounds were obtained from the experimental crystal structures. To calculate the TM dopants in ZnO, model structures were computed using the plane-wave-based projected augmented wave (PAW) method (VASP code). Space groups, lattice constants, cluster models, and TM-O bond lengths are summarized in Table I. To take account of the effective Madelung potential, an array of point charges was placed at the external atomic sites of clusters using the method proposed by Evjen.⁴⁵

Once molecular spinors were obtained, one-electron integrals $\langle i|\hat{h}|j\rangle$ and two-electron integrals $\langle ij|r_{12}^{-1}|kl\rangle$ were

directly evaluated over all possible combinations of ϕ_{2p}, ϕ_{3d} , and ϕ_{O-2p} molecular spinors by numerical integration, where ϕ_X denotes molecular spinors mainly composed of X atomic spinors.

C. Restriction of electronic configurations

After the one- and two-electron integrals were evaluated, Slater determinants were constructed as basis functions for many-electron wave functions. Because of the limited computational power, we restricted the number of Slater determinants. The simplest condition for TM- $L_{2,3}$ XANES/ELNES corresponds to the electronic transition from the $(\phi_{2p})^6(\phi_{3d})^n$ configuration to the $(\phi_{2p})^5(\phi_{3d})^{n+1}$ configuration, where n is the number of $3d$ electrons in a TM atom. The ϕ_{O-2p} spinors were fully occupied in these Slater determinants. Other core and valence electrons occupying the molecular spinors mainly composed of TM $1s, 2s, 3s$, and $3p$ and O $1s$ and $2s$ were treated as an effective potential within the

TABLE I. Lattice parameters and cluster models used in this work.

Compound	Space group	Lattice constant (Å, deg)	Cluster model		Point-group symmetry	TM-O bond length (Å)	Ref. no
TiO	$Fm\bar{3}m$	$a = 4.177$	TiO ₆ ¹⁰⁻	(d^2)	O_h	2.089	28
Ti ₂ O ₃	$R\bar{3}c$	$a = 5.157$ $c = 13.610$	TiO ₆ ⁹⁻	(d^1)	C_3	2.068 2.025	29 29
SrTiO ₃	$Pm\bar{3}m$	$a = 3.9050$	TiO ₆ ⁸⁻	(d^0)	O_h	1.953	30
VO	$Fm\bar{3}m$	$a = 4.073$	VO ₆ ¹⁰⁻	(d^3)	O_h	2.037	31
V ₂ O ₃	$R\bar{3}c$	$a = 4.9912$ $c = 13.9647$	VO ₆ ⁹⁻	(d^2)	C_3	2.061 1.975	32
VO ₂	$P4_2/mnm$	$a = 4.5540$ $c = 2.8557$	VO ₆ ⁸⁻	(d^1)	D_{2h}	1.974 1.857	33
CrO ^a	$Fm\bar{3}m$	$a = 4.1$	CrO ₆ ¹⁰⁻	(d^4)	O_h	2.05	
Cr ₂ O ₃	$R\bar{3}c$	$a = 4.96004$ $c = 13.5982$	CrO ₆ ⁹⁻	(d^3)	C_3	1.965 2.015	34
CrO ₂	$P4_2/mnm$	$a = 4.42193$ $c = 2.91659$	CrO ₆ ⁸⁻	(d^2)	D_{2h}	1.911 1.891	35
MnO	$Fm\bar{3}m$	$a = 4.444$	MnO ₆ ¹⁰⁻	(d^5)	O_h	2.222	36
ZnO:Mn ^b			MnO ₄ ⁶⁻	(d^5)	C_1	2.032 2.034	
LaMnO ₃	$Pnma$	$a = 5.6991$ $b = 7.7175$ $c = 5.5392$	MnO ₆ ⁹⁻	(d^4)	C_i	1.973 1.918 2.145	37
MnO ₂	$P4_2/mnm$	$a = 4.3983$ $c = 2.8730$	MnO ₆ ⁸⁻	(d^3)	D_{2h}	1.880 1.898	38
FeO	$Fm\bar{3}m$	$a = 4.3064$	FeO ₆ ¹⁰⁻	(d^6)	O_h	2.153	39
LaFeO ₃	$Pm\bar{3}m$	$a = 3.926$	FeO ₆ ⁹⁻	(d^5)	O_h	1.963	40
CoO	$Fm\bar{3}m$	$a = 4.2580$	CoO ₆ ¹⁰⁻	(d^7)	O_h	2.129	41
ZnO:Co ^b			CoO ₄ ⁶⁻	(d^7)	C_1	1.967 1.973	
LaCoO ₃	$R\bar{3}c$	$a = 5.3778$ $\alpha = 60.798$	CoO ₆ ⁹⁻	(d^6)	C_3	1.932 1.932	42
NiO	$Fm\bar{3}m$	$a = 4.1790$	NiO ₆ ¹⁰⁻	(d^8)	O_h	2.090	43
ZnO:Ni ^b			NiO ₄ ⁶⁻	(d^8)	C_1	1.941 1.985	

^aCr-O distance and lattice constants were determined from Shannon's ionic radii.⁴⁴

^bModel structures were obtained by plane-wave-based PAW method.

LDA. The configurations having two or more holes on ϕ_{2p} were not considered since the many-electron energies of such configurations are much higher and do not interact with the two configurations described above. Hereafter, we refer to this approach as the *ab initio* LFM approach.

For example, in MnO ($n = 5$), the number of Slater determinants for the initial configuration, $(\phi_{2p})^6(\phi_{3d})^5$, is 252 ($= {}_6C_6 \times {}_{10}C_5$), while that for the final configuration, $(\phi_{2p})^5(\phi_{3d})^6$, is 1260 ($= {}_6C_5 \times {}_{10}C_6$). The electronic configurations corresponding to the initial and final states of TM- $L_{2,3}$ XANES/ELNES and the numbers of Slater determinants for different $3d$ occupations are summarized in Table II.

The CT between ligands and TM atoms plays an important role in determining the spectral shapes of the TM- $L_{2,3}$ XANES/ELNES of some $3d$ TM compounds. In the case of $3d$ TM oxides, the most important CT channel is the electronic transition from ligand O- $2p$ to TM- $3d$ levels. In the *ab initio* LFM approach described above, part of this charge transfer through the covalent bonding between TM- $3d$ and O- $2p$ is automatically included by using molecular spinors instead of atomic ones. The other part of the CT effect can be included by considering the additional configurations (Slater determinants)

with a hole(s) on the ϕ_{O-2p} levels in the CI. We refer to this approach as the *ab initio* CTM approach.

In the case of MnO, $(\phi_{2p})^6(\phi_{O-2p})^{35}(\phi_{3d})^6$ and $(\phi_{2p})^5(\phi_{O-2p})^{35}(\phi_{3d})^7$ configurations were added to describe the initial and final states, respectively. The numbers of Slater determinants belonging to these configurations are 7560 ($= {}_6C_6 \times {}_{36}C_{35} \times {}_{10}C_6$) and 25 920 ($= {}_6C_5 \times {}_{36}C_{35} \times {}_{10}C_7$), respectively. This means that the number of multiplet levels contributing to the TM- $L_{2,3}$ XANES/ELNES also increases as the same number. The number of Slater determinants that belong to charge transferred configurations is also listed in Table II (only for the TMO₆ cluster). One can see that the number of Slater determinants drastically increases by including these configurations. The configurations having two or more holes on ϕ_{O-2p} levels were not considered in the present calculations.

It should be noted that the relativistic spinors optimized for the initial states were used to construct the Slater determinants corresponding to both the initial and the final states. In the many-electron scheme, the core-hole effects were included by considering the core-hole configurations in the CI calculations.

TABLE II. Occupation numbers of each level of spinors in the electronic configurations considered for calculations of TM- $L_{2,3}$ XANES using TMO₆ cluster models. The number of Slater determinants in each configuration (N_{SD}) is listed in the final column. Charge-transferred configurations are marked by asterisks.

		$\phi_{2p_{1/2}}$	$\phi_{2p_{3/2}}$	ϕ_{O-2p}	ϕ_{3d}	N_{SD}			$\phi_{2p_{1/2}}$	$\phi_{2p_{3/2}}$	ϕ_{O-2p}	ϕ_{3d}	N_{SD}	
d^0	Initial	2	4	36	0	1	d^5	Initial	2	4	36	5	252	
	*	2	4	35	1	360		*	2	4	35	6	7 560	
	Final	2	3	36	1	40		Final	2	3	36	6	840	
		1	4	36	1	20			1	4	36	6	420	
	*	2	3	35	2	6 480		*	2	3	35	7	17 280	
d^1	*	1	4	35	2	3 240	d^6	Initial	2	4	36	6	210	
	Initial	2	4	36	1	10		*	2	4	35	7	4 320	
	*	2	4	35	2	1 620		Final	2	3	36	7	480	
	Final	2	3	36	2	180			1	4	36	7	240	
		1	4	36	2	90		*	2	3	35	8	6 480	
d^2	*	2	3	35	3	17 280	d^7	*	1	4	35	8	3 240	
	*	1	4	35	3	8 640		Initial	2	4	36	7	120	
	Initial	2	4	36	2	45		*	2	4	35	8	1 620	
	*	2	4	35	3	4 320		Final	2	3	36	8	180	
	Final	2	3	36	3	480			1	4	36	8	90	
d^3		1	4	36	3	240	d^8	*	2	3	35	9	1 440	
	*	2	3	35	4	30 240		d^8	Initial	2	4	36	8	45
	*	1	4	35	4	15 120			*	2	4	35	9	360
	Initial	2	4	36	3	120			Final	2	3	36	9	40
	*	2	4	35	4	7 560				1	4	36	9	20
Final	2	3	36	4	840	*	2		3	35	10	144		
d^4		1	4	36	4	420	d^8	*	1	4	35	10	72	
	*	2	3	35	5	36 288		Initial	2	4	36	8	45	
	*	1	4	35	5	18 144		*	2	4	35	9	360	
	Initial	2	4	36	4	210		Final	2	3	36	9	40	
	*	2	4	35	5	9 072			1	4	36	9	20	
d^4	Final	2	3	36	5	1 008	d^8	*	2	3	35	10	144	
		1	4	36	5	504		d^8	*	1	4	35	10	72
	*	2	3	35	6	30 240			Initial	2	4	36	8	45
	*	1	4	35	6	15 120			*	2	4	35	9	360
	Final	2	3	36	5	1 008			Final	2	3	36	9	40
	1	4	36	5	504		1		4	36	9	20		

III. RESULTS AND DISCUSSION

A. Effects of covalency

As the first step of the CI calculations for the TM- $L_{2,3}$ XANES/ELNES of TM oxides, we made relativistic density-functional calculations within the LDA using the cluster models listed in Table I. The TM- $2p$ levels split into $2p_{1/2}$ and $2p_{3/2}$ because of the spin-orbit coupling. The energy separation between the L_3 and the L_2 edges is mainly ascribed to the spin-orbit splitting on the core $2p$ levels of the TM ion, ξ_{2p} . In TMO_6 clusters with octahedral symmetry (TMO_4 clusters with tetrahedral symmetry), TM- $3d$ levels split into t_{2g} (e) and e_g (t_2) levels. t_{2g} (e) and e_g (t_2) levels split further in the lower point group symmetry because of the distortion of the ligand field. The energy splitting on TM- $3d$ levels is affected by the crystal field and the covalency between TM- $3d$ and O- $2p$ spinors. ξ_{2p} and the averaged energy difference between the t_{2g} (e) and the e_g (t_2) levels, that is, $10Dq$, obtained by relativistic molecular spinor calculations are listed in Table III. ξ_{2p} is the same when the atomic number of the TM ion is the same and increases with the increase in atomic number of the TM ion. In contrast, $10Dq$ depends on the valency of the TM ion and the crystalline structure.

It is generally accepted that the magnitude of covalent bonding between TM- $3d$ and O- $2p$ increases with increasing formal charge and increasing atomic number of the TM element. To quantify the trend, Mulliken's population analysis⁴⁶ was performed. The averaged atomic spinor populations of O- $2p$ (Q_{O-2p}) in t_{2g} (e) and e_g (t_2) for $3d$ TM oxides are also listed

in Table III. The trend described above can be clearly seen in Table III. The O- $2p$ population is greater in e_g (t_2) than in t_{2g} (e). The O- $2p$ population in e_g exceeds 10% except for the divalent oxides of the former TM elements. In the case of high-valency oxides such as CrO_2 , MnO_2 , and LaCoO_3 , the O- $2p$ population in e_g is more than 15%. The results indicate that the inclusion of the covalency between oxygen and $3d$ TM elements is essential to calculate TM- $L_{2,3}$ XANES.

It should be noted that the expressions t_{2g} and e_g are not rigorously correct within relativistic theory. Instead, double-group expressions such as γ_{7g} (γ_{7g}^+) and γ_{8g} (γ_{8g}^+) should be employed. However, the relativistic effects for TM- $3d$ levels are small; thus, the expressions t_{2g} and e_g are subsequently adopted in this paper for simplicity.

After the density-functional calculations, the one-electron integrals $\langle i|\hat{h}|j\rangle$ and two-electron integrals $\langle ij|r_{12}^{-1}|kl\rangle$ among molecular spinors were computed. Because the multiplet levels are obtained as eigenvalues of the many-electron Hamiltonian in Eq. (1), the multiplet energies are determined by the values of those integrals. $\langle i|\hat{h}|j\rangle$ describes the ligand field splitting and the hopping integrals among molecular spinors, while $\langle ij|r_{12}^{-1}|kl\rangle$ denotes the interelectron interaction energies. Since those integrals are directly evaluated over molecular spinors, they are strongly affected by the covalency and the crystal field.

In Table III, the calculated two-electron integrals are also shown. Although we obtained the values of all $\langle ij|r_{12}^{-1}|kl\rangle$ terms, only the averaged value of Coulomb

TABLE III. Spin-orbit splitting on core $2p$ levels, ξ_{2p} ; averaged energy difference between t_{2g} and e_g levels, i.e., $10Dq$; Mulliken's O- $2p$ atomic spinor populations of t_{2g} , $Q_{O-2p}(t_{2g})$, and e_g , $Q_{O-2p}(e_g)$, obtained by relativistic molecular spinor calculations; averaged Coulomb integrals $\langle ij|r_{12}^{-1}|ij\rangle$ ($i \neq j$) between ϕ_{2p} and ϕ_{3d} [$U_{\text{ave}}(\phi_{2p}\phi_{3d})$]; and those among ϕ_{3d} [$U_{\text{ave}}(\phi_{3d}\phi'_{3d})$]. Values in parentheses indicate the ratios between the U_{ave} for clusters and that for isolated TM ions. The final column lists the compositions of the charge-transferred configuration in the many-electron wave function corresponding to the initial state of TM- $L_{2,3}$ XANES.

Compound	ξ_{2p} (eV)	$10Dq$ (eV)	Mulliken's population		Coulomb integral		Composition of CT configuration
			$Q_{O-2p}(t_{2g})$	$Q_{O-2p}(e_g)$	$U_{\text{ave}}(\phi_{2p}\phi_{3d})$ (eV)	$U_{\text{ave}}(\phi_{3d}\phi'_{3d})$ (eV)	
TiO	5.78	2.02	0.020	0.059	25.28(0.975)	17.73(0.953)	0.020
Ti ₂ O ₃	5.78	2.03	0.024	0.103	26.03(0.937)	18.19(0.898)	0.033
SrTiO ₃	5.78	2.24	0.083	0.126	26.31(0.888)	18.12(0.829)	0.050
VO	7.11	1.99	0.022	0.066	27.10(0.975)	18.89(0.951)	0.024
V ₂ O ₃	7.11	1.93	0.036	0.114	27.72(0.934)	19.24(0.893)	0.041
VO ₂	7.11	2.36	0.074	0.160	27.87(0.885)	18.97(0.818)	0.052
CrO	8.65	1.72	0.022	0.073	28.78(0.969)	19.93(0.942)	0.029
Cr ₂ O ₃	8.65	1.83	0.040	0.129	29.26(0.926)	20.96(0.880)	0.054
CrO ₂	8.65	2.28	0.079	0.176	29.22(0.875)	19.67(0.803)	0.059
MnO	10.44	1.10	0.022	0.083	30.16(0.953)	20.68(0.921)	0.047
LaMnO ₃	10.44	1.69	0.063	0.141	30.37(0.907)	20.44(0.846)	0.064
MnO ₂	10.44	2.25	0.095	0.198	30.37(0.860)	20.12(0.779)	0.073
FeO	12.50	1.14	0.023	0.091	31.97(0.953)	22.56(0.918)	0.047
LaFeO ₃	12.50	1.78	0.068	0.158	32.00(0.904)	21.42(0.840)	0.072
CoO	14.84	1.14	0.027	0.111	33.64(0.948)	22.78(0.908)	0.059
LaCoO ₃	14.84	1.79	0.072	0.182	33.36(0.894)	22.13(0.825)	0.077 ^a
NiO	17.50	1.19	0.033	0.143	35.13(0.939)	23.53(0.890)	0.084
ZnO:Mn	10.44	0.52	0.029(e)	0.062(t_2)	29.83(0.943)	20.38(0.907)	0.052
ZnO:Co	14.84	0.58	0.044(e)	0.094(t_2)	33.11(0.933)	22.23(0.886)	0.063
ZnO:Ni	17.50	0.52	0.058(e)	0.124(t_2)	34.35(0.918)	22.69(0.859)	0.084

^aOnly low-spin configurations were considered for the initial state.

integrals, $\langle ij|r_{12}^{-1}|ij\rangle$, between ϕ_{2p} and ϕ_{3d} molecular spinors $[U_{\text{ave}}(\phi_{2p}\phi_{3d})]$ and those among ϕ_{3d} molecular spinors $[U_{\text{ave}}(\phi_{3d}\phi'_{3d})]$ are shown for simplicity. The values in parentheses in Table III are the ratios between the $U_{\text{ave}}(\phi_{2p}\phi_{3d})$ $[U_{\text{ave}}(\phi_{3d}\phi'_{3d})]$ of cluster models and the corresponding integrals for isolated TM ions with the same formal charges. Note that for an isolated atom, those integrals are single-center integrals and can be decomposed as the sum of Slater integrals, that is, F^0 , F^2 , and F^4 multiplied by the integrals of the angular part. For molecules or cluster models composed of multiple atoms, they are two-center integrals which cannot be described as a simple weighted sum of Slater integrals. In the present calculations, $\langle ij|r_{12}^{-1}|kl\rangle$ over molecular spinors are directly evaluated by numerical integration.

From Table III, one can see that both $U_{\text{ave}}(\phi_{2p}\phi_{3d})$ and $U_{\text{ave}}(\phi_{3d}\phi'_{3d})$ increase with increasing atomic number of the TM ion. This is because both $2p$ and $3d$ electrons are bounded strongly and localized around the nucleus when atomic number increases. One can also find that those integrals are reduced from the atomic values in all oxides. This is ascribed to the strong covalent bonding between TM- $3d$ and O- $2p$ in $3d$ TM oxides. The TM- $3d$ spinors spatially spread when O- $2p$ spinors are mixed in, which results in the reduction of interelectron interactions.

It should also be noted that the reduction factors differ in each level, reflecting the difference in covalency. The reduction factors for $U_{\text{ave}}(\phi_{2p}\phi_{3d})$ are larger than those for $U_{\text{ave}}(\phi_{3d}\phi'_{3d})$ as reported in Table III, because TM- $2p$ atomic spinors are hardly affected by ligand atoms. In addition, the reduction factors of $U_{\text{ave}}(t_{2g}, t'_{2g})$ become smaller than those of $U_{\text{ave}}(e_g, e'_g)$ in the case of a TMO₆ cluster (not shown in Table III). This is because the O- $2p$ population is larger in e_g than in t_{2g} (see Refs. 19 and 20).

B. Charge transfer effects on TM- $L_{2,3}$ XANES

1. Initial state

A LFM and *ab initio* CTM calculations were systematically performed for $3d$ TM oxides listed in Table I. First, we show the results for the initial states. In the *ab initio* LFM calculations, only the $(\phi_{2p})^6(\phi_{3d})^n$ configuration was considered to describe the initial state of TMO₆ (TMO₄) clusters. In the *ab initio* CTM calculations, the charge-transferred configuration, that is, $(\phi_{2p})^6(\phi_{O-2p})^{35}(\phi_{3d})^{n+1}$ for the TMO₆ cluster and $(\phi_{2p})^6(\phi_{O-2p})^{23}(\phi_{3d})^{n+1}$ for the TMO₄ cluster, was considered in addition to the previous configurations. These configurations interact with each other and change the wave function at the initial state. This is the CT effect, which is separate from the effect of covalency in the initial state of TM- $L_{2,3}$ XANES. The composition of the charge-transferred configuration in the initial state obtained by *ab* CTM calculation is also reported in Table III. The strong correlation between the O- $2p$ population (Q_{O-2p}) and the composition of the charge-transferred configuration can be seen. The composition of the charge-transferred configuration increases with increasing valency for a given atomic number of the TM element and increases with increasing atomic number of the TM element for a given valency of the TM.

It should be noted that the composition of the charge-transferred configuration in the initial state in the *ab initio*

CTM calculation is much smaller than the composition of $2p^63d^{n+1}\underline{L}$ in the semiempirical CTM method. This is because the covalency is already included by using the molecular spinors (ϕ_{3d}) instead of the atomic spinors ($3d$) in the former case, while it is included through the mixing of the $2p^63d^{n+1}\underline{L}$ configuration in the latter case.

2. Charge transfer effects on spectra

The lower panels in Figs. 1–7 show the theoretical PACS of $3d$ TM oxides obtained by the *ab initio* LFM approach (gray line) and the *ab initio* CTM approach (black line). We found that in many compounds, the transition energy obtained by the *ab initio* CTM approach was about 1–2 eV higher than that obtained using the LFM approach. In Figs. 1–7, the theoretical spectra obtained by the *ab initio* CTM approach are shifted to align the most significant L_3 peak of the two theoretical spectra for easy comparison. In LaCoO₃, it is known that the Co ions are trivalent, with low-spin states in the ground state.^{57–60} In the calculation of LaCoO₃, only the configurations corresponding to the low-spin state, that is, $(\phi_{2p})^6(\phi_{O-2p})^{36}(t_{2g})^6(e_g)^0$ and $(\phi_{2p})^6(\phi_{O-2p})^{35}(t_{2g})^6(e_g)^1$, are used for the initial state to enforce the low-spin state in the initial state. The experimental spectra (upper panels in Figs. 1–7), measured by the present authors or taken from the literature,^{47–57} are also shown for comparison. Good experimental spectra were not found for TiO, CrO, or VO. Experimental spectra for ZnO:Mn, NiO, and ZnO:Ni were measured by the present authors at BL25SU in SPring-8 (Harima, Japan).

The difference between the two theoretical spectra (gray and black lines) in each figure is fully ascribed to the CT from ϕ_{O-2p} to ϕ_{3d} . In the divalent oxides of Ti, V, Cr, Mn, and Fe, the theoretical spectra obtained by the *ab initio* LFM and *ab initio* CTM have identical line shapes. This means that they are hardly affected by the CT (Figs. 2–5). Small changes in peak intensities can be observed at the Co $L_{2,3}$ edges of CoO and ZnO:Co upon inclusion of the CT (Fig. 6). In contrast, a clear difference between the two theoretical spectra can be seen in the case of Ni oxides (Fig. 7). For NiO, the intensity of the Ni- L_2 peaks increases and the double-peak structure becomes much clearer upon including the CT. Meantime, the intensity of the main L_3 peak decreases while that of the shoulder peak located at a higher energy increases. In ZnO:Ni, the main L_3 peak becomes sharper, and the intensities of the two L_2 peaks are inverted. The agreement between the experiment and theory is much better when the CT is included. Thus, the CT is essential in interpreting the Ni- $L_{2,3}$ spectra of Ni oxides.

The discrepancies between the two theoretical spectra become larger with increasing valency of the TM. In the case of Ti₂O₃ and V₂O₃, the intensities of the L_2 peaks were slightly changed by including the CT (Figs. 1 and 2). The intensity of the top peak at the Cr L_2 -edge from Cr₂O₃ decreases when the CT is considered (Fig. 3). In addition, the intensities of the Cr- L_3 peaks are also affected by the CT. The results indicate that the CT is not negligible even for trivalent oxides of the former TMs, that is, Ti, V, and Cr. The effect of the CT becomes larger for the latter TM oxides, that is, Mn, Fe, and Co. In the case of LaMnO₃, the Mn L_3 edge changes markedly upon inclusion of the CT. This is due to the strong CI among $(\phi_{2p_{1/2}})^2(\phi_{2p_{3/2}})^3(\phi_{O-2p})^{36}(\phi_{3d})^4$ and $(\phi_{2p_{1/2}})^2(\phi_{2p_{3/2}})^3(\phi_{O-2p})^{35}(\phi_{3d})^5$ in the final states, which

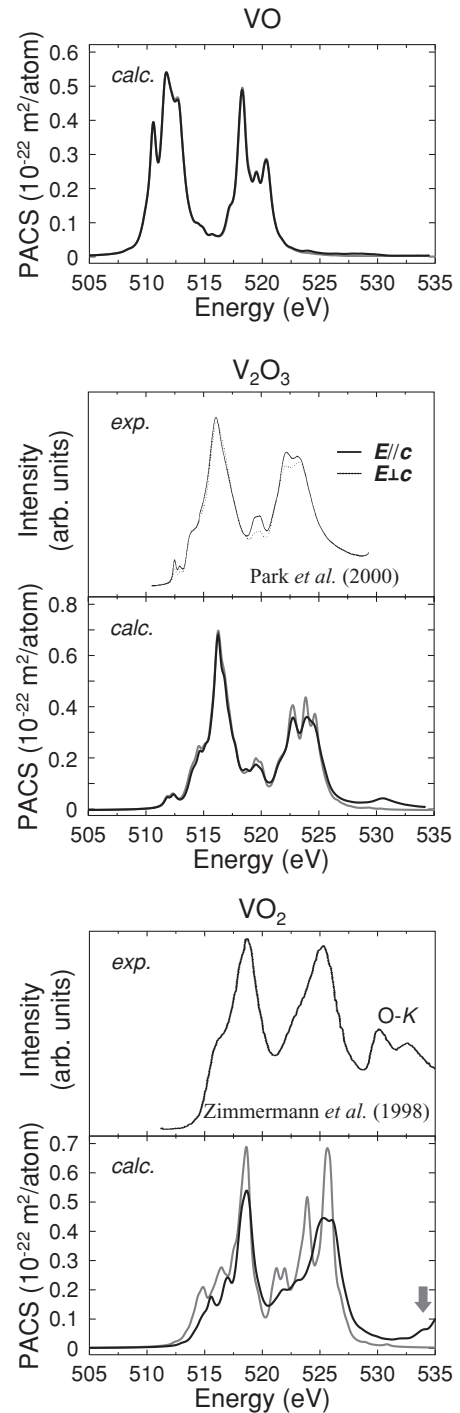
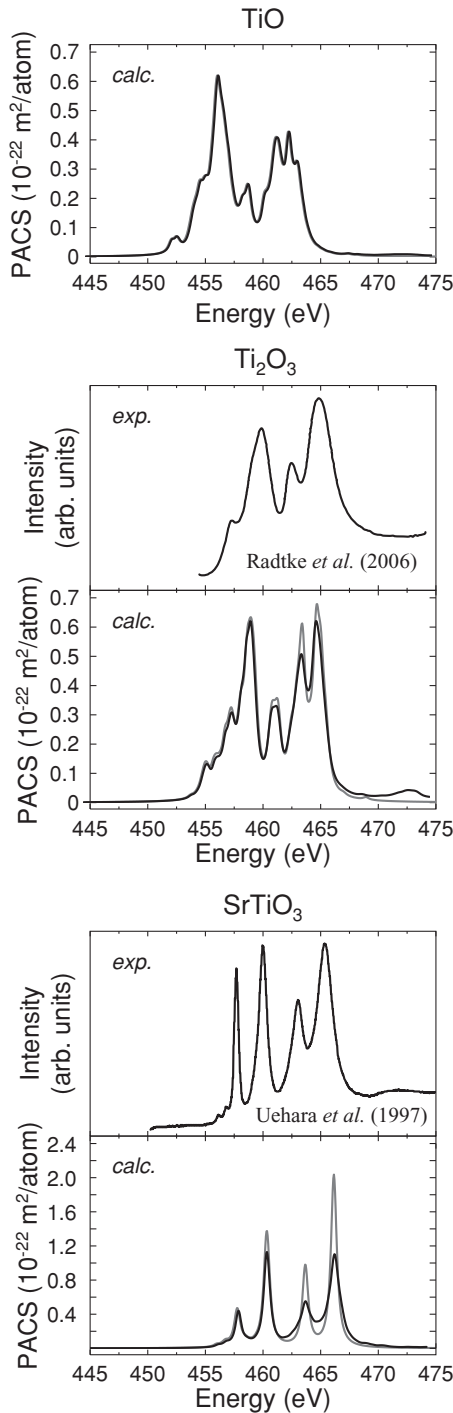


FIG. 1. Theoretical Ti- $L_{2,3}$ XANES of TiO (Ti^{2+}), Ti_2O_3 (Ti^{3+}), and $SrTiO_3$ (Ti^{4+}) obtained by the *ab initio* LFM approach (gray lines) and CTM approach (black lines). Experimental spectra taken from the literature^{47,48} are also shown for comparison except for TiO.

FIG. 2. Theoretical V- $L_{2,3}$ XANES of VO (V^{2+}), V_2O_3 (V^{3+}), and VO_2 (V^{4+}) obtained by the *ab initio* LFM approach (gray lines) and CTM approach (black lines). Experimental spectra taken from the literature^{49,50} are also shown for comparison except for VO. Note that the peaks indicated by arrows in this and subsequent figures are considered to be artifacts, as discussed in Sec. IV.

contributes to the L_3 peaks. In the case of $LaCoO_3$, the intensity ratio between the main peak and the shoulder peak located at a higher energy is changed upon inclusion of the CT effect not only on the Co L_2 edge but also on the Co L_3 edge.

For tetravalent oxides, TM- $L_{2,3}$ XANES are strongly modified by the CT even for the former TM oxides. For instance, the Ti- L_2 peaks of $SrTiO_3$ are broadened by including the CT. The intensity ratio between the two main L_3 peaks

is also changed (Fig. 1). It should be noted that the extra broadening of the L_2 peaks in $SrTiO_3$ has been explained by the shorter lifetime of the core hole in $2p_{1/2}$ than in $2p_{3/2}$ and by Coster-Kronig Auger decay.⁶¹ The present result clearly shows that the CT from the ligand oxygen to the Ti ion also contributes to the broadening of the L_2 peaks in $SrTiO_3$. The

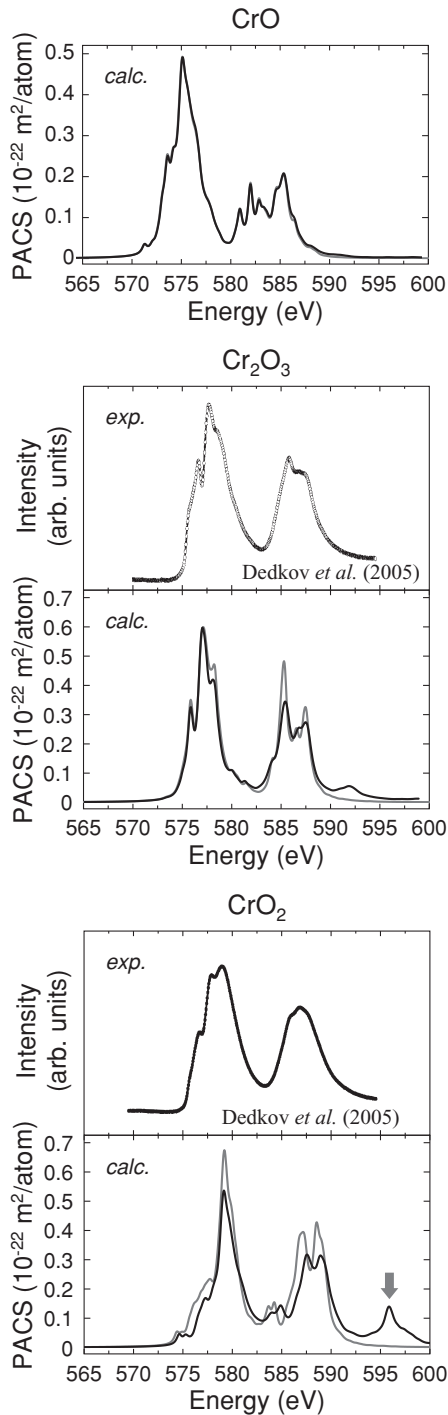


FIG. 3. Theoretical Cr- $L_{2,3}$ XANES of CrO (Cr²⁺), Cr₂O₃ (Cr³⁺), and CrO₂ (Cr⁴⁺) obtained by the *ab initio* LFM approach (gray lines) and CTM approach (black lines). Experimental spectra taken from the literature⁵¹ are also shown for comparison except for CrO. Note that, according to Ref. 51, the surface of CrO₂ might be covered by a thin Cr₂O₃ layer.

V L_3 edge of VO₂ contracts slightly when the CT is taken into account (Fig. 2). The shapes and intensities of the V- L_2 peaks are considerably different between the two theoretical spectra of VO₂. The results indicate that the CT is essential for the

analysis of TM- $L_{2,3}$ XANES spectra when the valency of the TM is larger than +2.

IV. LIMITATIONS AND OUTLOOK

In the present work, CI calculations were performed using molecular spinors with relativistic density-functional theory. In order not to increase the computational cost to a prohibitive level, only a limited number of molecular spinors and electronic configurations were used in the CI calculations. Therefore, the quality of the theoretical spectra strongly depends on the quality of molecular spinors and the choice of electronic configurations.

In the calculations in the present work, we used small cluster models composed of only a TM ion and the nearest-neighboring ligands embedded in the raw Madelung potentials. Nevertheless, the TM- $L_{2,3}$ XANES of ionic compounds such as MnO were reproduced very well (Figs. 1–7). This is because, in ionic compounds, ϕ_{2p} and ϕ_{3d} spinors are well localized around the nucleus of the TM ion. Hence, the initial-state wave function is expected to be localized around the nucleus of the TM ion. The final-state wave functions should be further localized because of the creation of a core hole. Thus, molecular spinors using a small cluster are sufficient to reproduce the localized wave functions.

In the case of highly covalent extended systems, however, large discrepancies between experiment and theory were found. This can be partly ascribed to the insufficient treatment of the solid-state effects, which cannot be described by a small cluster model. A typical example of this is the Ti- $L_{2,3}$ XANES of TiO₂. Figure 8 shows the theoretical Ti- $L_{2,3}$ XANES of rutile TiO₂ calculated using a TiO₆⁸⁻ cluster model compared with an experimental spectrum.⁶² We can clearly see that the shoulder of the second main L_3 peak, located around 460 eV, is absent in the theoretical spectra, even after including the CT. The origin of this peak used to be ascribed to the splitting of e_g levels due to the tetragonal distortion of the TiO₆ octahedron in the rutile structure.⁶³ However, the e_g splitting obtained in the present calculation is 0.11 eV, which is too small to reproduce the splitting in the experimental spectrum. Very recently, Krüger applied the MCMS method to the Ti- $L_{2,3}$ XANES of SrTiO₃, rutile, and anatase TiO₂ and succeeded in reproducing the doublet structure using a large cluster model of about 60 atoms.²³ Our result in Fig. 8 is consistent with the MCMS results with a seven-atom cluster. Laskowski and Blaha also applied an all-electron BSE method based on APW + *lo* to the Ti- $L_{2,3}$ edge of TiO₂ and succeeded in reproducing the experimental spectra.²⁵ These results indicate that the doublet structure of this shoulder peak is due to solid-state effects.

To include the solid-state effects in the CI method, we have to use a larger cluster model. However, this is difficult in practice because the number of Slater determinants to be considered becomes too large. For instance, in the *ab initio* CTM calculation with the Ti₉O₅₀⁶⁴⁻ cluster, the number of Slater determinants is more than 7×10^7 , and the full diagonalization of such a large matrix is much too challenging with the current computational power available. This is the biggest drawback of the CI method in comparison with the MCMS and BSE methods. The disadvantage of the MCMS and the BSE methods is the technical difficulty in dealing with the

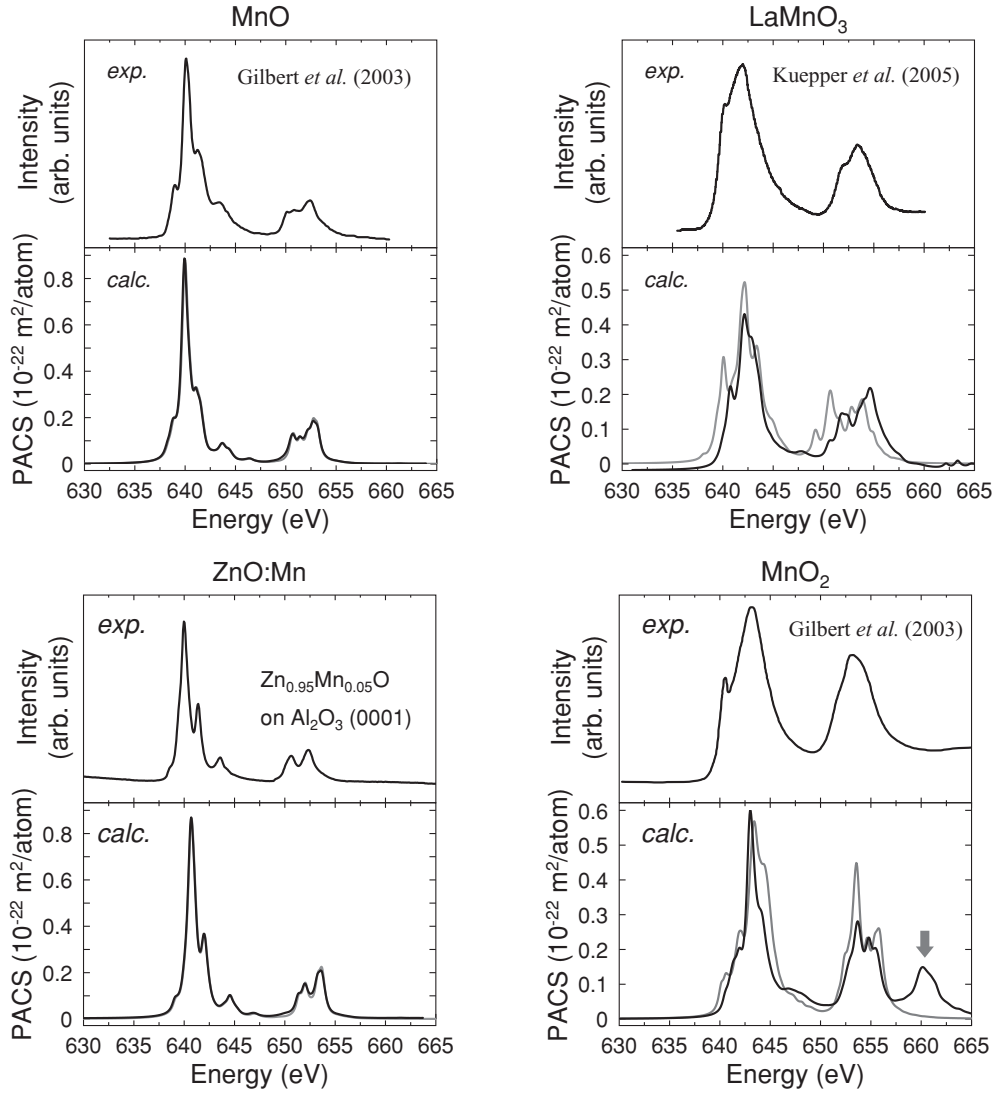


FIG. 4. Theoretical Mn- $L_{2,3}$ XANES of MnO (Mn^{2+} , CN = 6), Mn dopant in ZnO (Mn^{2+} , CN = 4), $LaMnO_3$ (Mn^{3+}), and MnO_2 (Mn^{4+}) obtained by the *ab initio* LFM approach (gray lines) and CTM approach (black lines). Experimental spectra measured or taken from the literature^{52,53} are also shown for comparison.

partly filled $3d$ systems, in which further multiplet effects among the $3d$ electrons should be properly taken into account.

One can see in Figs. 2–6 that some additional peaks not found in the experimental spectra appear in the theoretical spectra obtained by the *ab initio* CTM method. The intensities of the peaks are unrealistically strong in some tetravalent TM oxides. These peaks are indicated by arrows in the figures. They are considered to be artifacts due to the restriction of electronic configurations in the CI calculation. Let us discuss the origin of the artifacts in more detail. Figure 9 shows the theoretical Cr- $L_{2,3}$ XANES of CrO_2 (top; black line) which is decomposed into the contributions of the L_3 transition ($\phi_{2p_{3/2}} \rightarrow \phi_{3d}$) (top; red line), the L_2 transition ($\phi_{2p_{1/2}} \rightarrow \phi_{3d}$) (top; blue line), and their cross term (top; dashed green line). One can clearly see that the artifact located at about 595 eV can be mainly ascribed to the L_3 transition. The middle and lower panels in Fig. 9 show the compositions of four different electronic configurations in the

final states of the Cr- $L_{2,3}$ XANES, which are distinguished by different colors in the figure. The initial state of the Cr $L_{2,3}$ edges is dominated by the $(\phi_{2p_{1/2}})^2(\phi_{2p_{3/2}})^4(\phi_{O-2p})^{36}(\phi_{3d})^2$ configuration. Therefore, one can expect that two kinds of electronic configurations, that is, $(\phi_{2p_{1/2}})^2(\phi_{2p_{3/2}})^3(\phi_{O-2p})^{36}(\phi_{3d})^3$ (green bars) and $(\phi_{2p_{1/2}})^1(\phi_{2p_{3/2}})^4(\phi_{O-2p})^{36}(\phi_{3d})^3$ (red bars), mainly contribute to the oscillator strengths in the final states, and the two kinds of CT configurations in the final state, that is, $(\phi_{2p_{1/2}})^2(\phi_{2p_{3/2}})^3(\phi_{O-2p})^{35}(\phi_{3d})^4$ (blue bars) and $(\phi_{2p_{1/2}})^1(\phi_{2p_{3/2}})^4(\phi_{O-2p})^{35}(\phi_{3d})^4$ (orange bars), hardly contribute to the oscillator strengths. However, they contribute to the change in the multiplet structure by mixing with the former two non-CT configurations. It is clearly shown in Fig. 9 that the composition of the $(\phi_{2p_{1/2}})^2(\phi_{2p_{3/2}})^3(\phi_{O-2p})^{36}(\phi_{3d})^3$ configuration exceeds 10% for eigenstates corresponding to artifact peaks at around 595 eV, even though the transition energies are higher than the main L_2 line. The results indicate that unrealistic eigenstates are formed in this energy region.

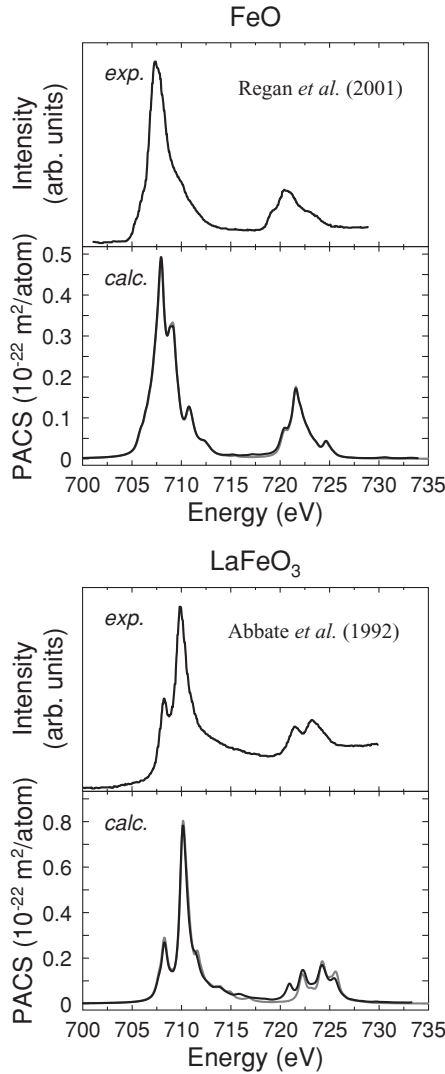


FIG. 5. Theoretical Fe- $L_{2,3}$ XANES of FeO (Fe^{2+}), LaFeO_3 (Fe^{3+}), and SrFeO_3 (Fe^{4+}) obtained by the *ab initio* LFM approach (gray lines) and CTM approach (black lines). Experimental spectra taken from the literature^{54,55} are also shown for comparison.

This could be ascribed to the incompleteness of the basis functions (Slater determinants) for many-electron eigenstates in the present calculation. If additional electronic configurations such as $(\phi_{2p})^5(\phi_{O-2p})^{34}(\phi_{3d})^5$ and $(\phi_{2p})^5(\phi_{3d})^2(\phi_{4sp})^1$ are considered, they could mainly interact with the eigenstates above the main L_2 line. As a result of such interactions, the contribution of the $(\phi_{2p_{1/2}})^2(\phi_{2p_{3/2}})^3(\phi_{O-2p})^{36}(\phi_{3d})^3$ configuration would be distributed over a wider energy region, and hence, the artifact peaks would become much broader and less visible.

V. CONCLUSIONS

The TM- $L_{2,3}$ XANES/ELNES of 3d TM oxides have been systematically calculated by the *ab initio* LFM and *ab initio* CTM approaches. In the *ab initio* LFM approach, only the $(\phi_{2p})^6(\phi_{3d})^n$ and $(\phi_{2p})^5(\phi_{3d})^{n+1}$ configurations have been considered in describing the initial and final states of TM- $L_{2,3}$ XANES/ELNES, respectively. In the *ab initio* CTM approach,

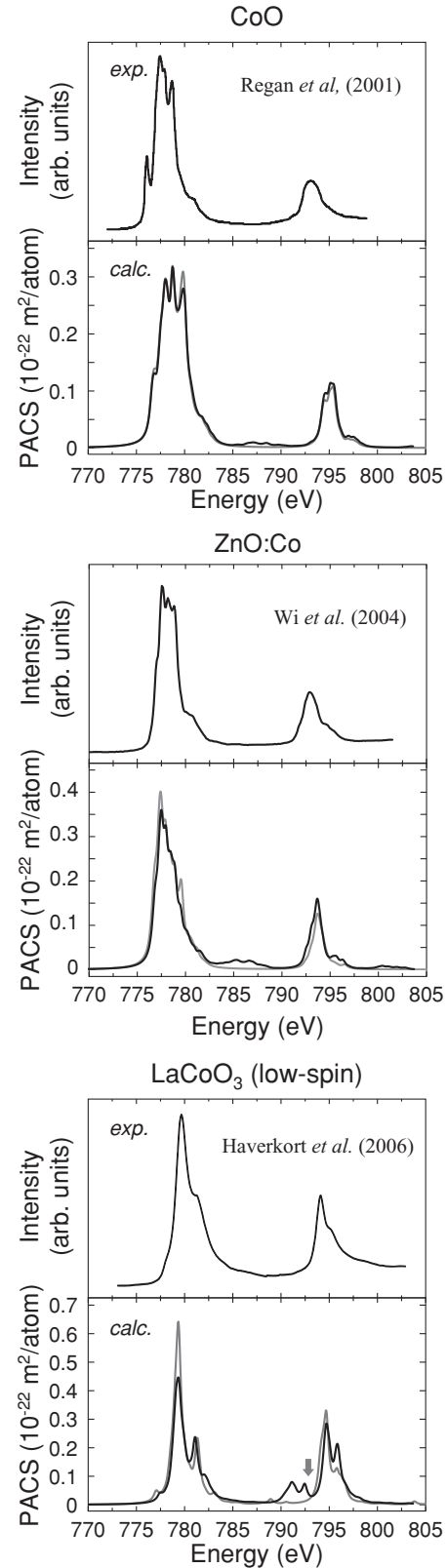


FIG. 6. Theoretical Co- $L_{2,3}$ XANES of CoO (Co^{2+} , CN=6), Co dopant in ZnO (Co^{2+} , CN=4), and LaCoO_3 (Co^{3+}) obtained by the *ab initio* LFM approach (gray lines) and CTM approach (black lines). In the calculations of LaCoO_3 , only the configurations corresponding to the low-spin state, i.e., $(\phi_{2p})^6(\phi_{O-2p})^{36}(t_{2g})^6(e_g)^0$ and $(\phi_{2p})^6(\phi_{O-2p})^{35}(t_{2g})^6(e_g)^1$, are used for the initial state. Experimental spectra taken from the literature^{54,56,57} are also shown for comparison.

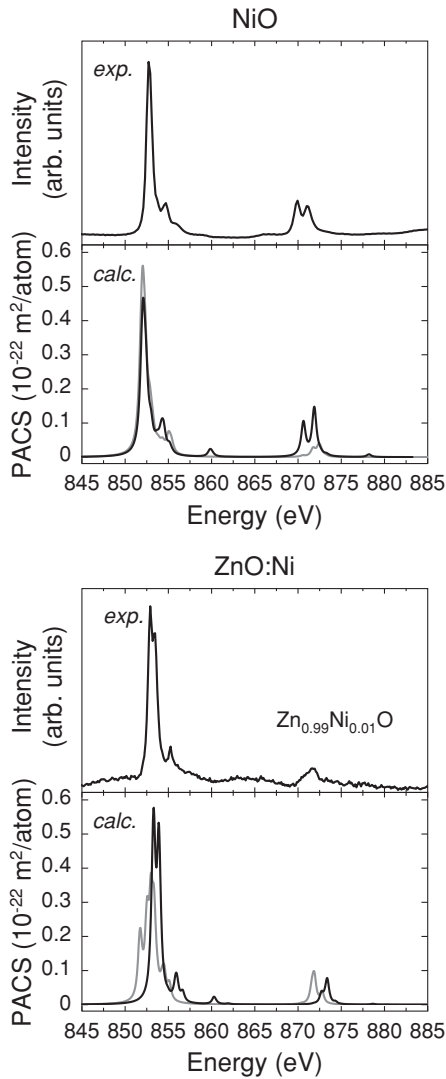


FIG. 7. Theoretical TM- $L_{2,3}$ XANES of NiO (Ni^{2+} ; CN = 6) and Ni dopant in ZnO (Ni^{2+} ; CN = 4) obtained by the *ab initio* LFM approach (gray lines) and CTM approach (black lines). Experimental spectra are also shown for comparison.

the charge-transferred configuration in which a ϕ_{O-2p} electron transferred into ϕ_{3d} has been included in the CI.

First, the influences of the covalency on TM $L_{2,3}$ -edges have been discussed. Since molecular spinors were used to construct Slater determinants, all ligand field effects including the crystal field and covalency were automatically included. The covalent bonding between TM elements and oxygen increased the spatial distribution of TM-3d spinors, which resulted in the reduction of interelectron interaction energies among TM-2p and 3d electrons. Hence, it changed the multiplet structures and the transition probabilities in the TM- $L_{2,3}$ XANES/ELNES.

After that, the influences of the CT on TM $L_{2,3}$ edges have been discussed. In the *ab initio* CTM approach, the contribution of the charge-transferred configuration increased with increasing atomic number and valency of TM ions in the oxides. This tendency is similar to that of the covalent bonding between TM-3d and O-2p spinors. The stronger the covalency, the larger the influence of the CT on TM- $L_{2,3}$ XANES/ELNES.

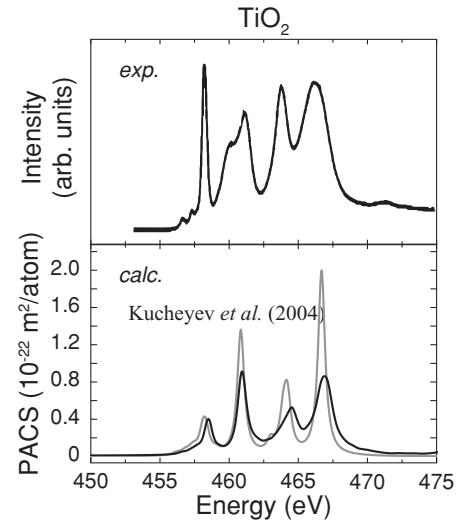


FIG. 8. Theoretical Ti- $L_{2,3}$ XANES of rutile TiO_2 (Ti^{4+} , CN = 6) obtained by the *ab initio* LFM approach (gray lines) and CTM approach (black lines). An experimental spectrum taken from the literature⁶² is also shown for comparison.

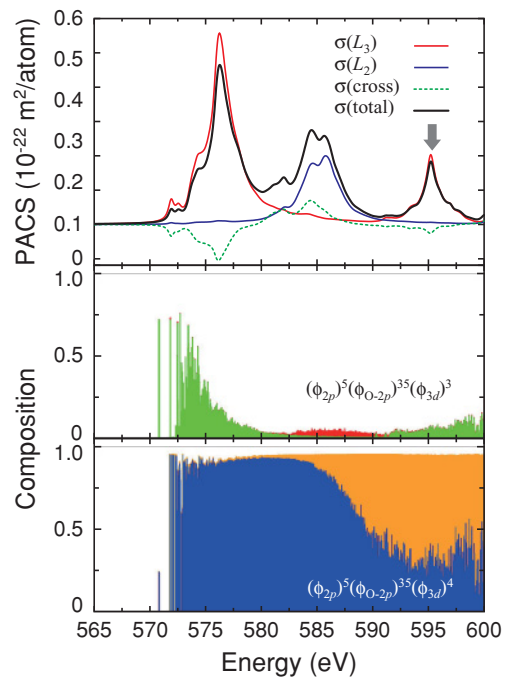


FIG. 9. (Color online) Top: Theoretical Cr- $L_{2,3}$ XANES of CrO_2 obtained by the *ab initio* CTM approach (black line). The spectrum is decomposed into the contributions of the L_3 ($\phi_{2p_{3/2}} \rightarrow \phi_{3d}$) transition channel (red line), the L_2 ($\phi_{2p_{1/2}} \rightarrow \phi_{3d}$) transition channel (blue line), and their cross term (dashed green line). Middle and bottom: Compositions of $(\phi_{2p})^5(\phi_{O-2p})^{36}(\phi_{3d})^3$ and $(\phi_{2p})^5(\phi_{O-2p})^{35}(\phi_{3d})^4$ configurations for many-electron eigenstates, respectively, where the contributions of L_3 and L_2 configurations are distinguished by different colors: green, $(\phi_{2p_{1/2}})^2(\phi_{2p_{3/2}})^3(\phi_{O-2p})^{36}(\phi_{3d})^3$; red, $(\phi_{2p_{1/2}})^1(\phi_{2p_{3/2}})^4(\phi_{O-2p})^{36}(\phi_{3d})^3$; blue $(\phi_{2p_{1/2}})^2(\phi_{2p_{3/2}})^3(\phi_{O-2p})^{35}(\phi_{3d})^4$; and orange, $(\phi_{2p_{1/2}})^1(\phi_{2p_{3/2}})^4(\phi_{O-2p})^{35}(\phi_{3d})^4$.

The TM- $L_{2,3}$ XANES/ELNES of 3d-TM oxides were calculated systematically by the *ab initio* LFM and *ab initio* CTM approaches. In the case of divalent oxides of Ti, V, Cr, Mn, and Fe, the spectral shapes were hardly affected by the CT; it was only necessary to take the CT into account for divalent Ni oxides. The effects of the CT on $L_{2,3}$ edges became larger when the valency of the TM increased. The CT mainly contributed to the changes in peak intensities and peak broadness and to the formation of satellite peaks.

Theoretical spectra of ionic compounds obtained by the *ab initio* CTM approach showed good agreement with the experimental results in general. The limitations to the present method are the absence of solid-state effects and the restriction of the electronic configurations.

At present, there is no universal method for simulating the $L_{2,3}$ -edge XANES/ELNES of all 3d TM compounds in an

ab initio manner. In particular, representation of the TM- $L_{2,3}$ XANES/ELNES of highly covalent or metallic systems with a partly filled 3d shell by an entirely nonempirical method is still challenging. Further progress in developing suitable theories and algorithms is essential.

ACKNOWLEDGMENTS

This study was supported by Grant-in-Aid for Scientific Research on Priority Areas “Nano Materials Science for Atomic Scale Modification 474” and Young Scientists (A) No. 22686059 from the Ministry of Education, Culture, Sports, Science and Technology (MEXT) of Japan. XANES measurements were performed at BL25SU in SPring-8 under Proposal No. 2008A1516.

*Corresponding author: ikeno@fukui.kyoto-u.ac.jp

¹D. C. Koningsberger and R. Prins (eds.), *X-Ray Absorption: Principles, Applications, Techniques of EXAFS, SEXAFS and XANES, Chemical Analysis: A Series of Monographs on Analytical Chemistry and Its Applications* (John Wiley & Sons, New York, 1988).

²R. Egerton (ed.), *Electron Energy-Loss Spectroscopy in the Electron Microscopy* (Plenum Press, New York, 1996).

³J. Stöhr, *NEXAFS Spectroscopy, Springer Series in Surface Sciences* (Springer Verlag, Berlin, 1992).

⁴J. G. Chen, *Surf. Sci. Rep.* **30**, 1 (1997).

⁵J. J. Rehr and R. C. Albers, *Rev. Mod. Phys.* **72**, 621 (2000).

⁶A. Filipponi, A. Di Cicco, and C. R. Natoli, *Phys. Rev. B* **52**, 15122 (1995).

⁷A. Filipponi and A. Di Cicco, *Phys. Rev. B* **52**, 15135 (1995).

⁸T. Mizoguchi, I. Tanaka, S. Yoshioka, M. Kunisu, T. Yamamoto, and W. Y. Ching, *Phys. Rev. B* **70**, 045103 (2004).

⁹I. Tanaka, T. Mizoguchi, and T. Yamamoto, *J. Am. Ceram. Soc.* **88**, 2013 (2005).

¹⁰T. Mizoguchi, W. Olovsson, H. Ikeno, and I. Tanaka, *Micron* **41**, 695 (2010).

¹¹F. de Groot, *Coord. Chem. Rev.* **249**, 31 (2005).

¹²F. M. F. de Groot, *J. Electron Spectrosc. Relat. Phenom.* **67**, 529 (1994).

¹³A. Kotani, *J. Electron Spectrosc. Relat. Phenom.* **100**, 75 (1999).

¹⁴F. de Groot and A. Kotani, *Core Level Spectroscopy of Solids, Advances in Condensed Matter Science* (CRC Press, Boca Raton, FL, 2008).

¹⁵K. Ogasawara, T. Iwata, Y. Koyama, T. Ishii, I. Tanaka, and H. Adachi, *Phys. Rev. B* **64**, 115413 (2001).

¹⁶H. Ikeno, I. Tanaka, Y. Koyama, T. Mizoguchi, and K. Ogasawara, *Phys. Rev. B* **72**, 075123 (2005).

¹⁷H. Ikeno, T. Mizoguchi, Y. Koyama, Y. Kumagai, and I. Tanaka, *Ultramicroscopy* **106**, 970 (2006).

¹⁸Y. Kumagai, H. Ikeno, F. Oba, K. Matsunaga, and I. Tanaka, *Phys. Rev. B* **77**, 155124 (2008).

¹⁹H. Ikeno, F. M. F. de Groot, E. Stavitski, and I. Tanaka, *J. Phys. Condens. Matter* **21**, 104208 (2009).

²⁰H. Ikeno, F. M. F. de Groot, and I. Tanaka, *J. Phys. Conf. Series* **190**, 012005 (2009).

²¹C. R. Natoli, M. Benfatto, C. Brouder, M. F. Ruiz López, and D. L. Foulis, *Phys. Rev. B* **42**, 1944 (1990).

²²P. Krüger and C. R. Natoli, *Phys. Rev. B* **70**, 245120 (2004).

²³P. Krüger, *Phys. Rev. B* **81**, 125121 (2010).

²⁴E. L. Shirley, *J. Electron Spectrosc. Relat. Phenom.* **144-147**, 1187 (2005).

²⁵R. Laskowski and P. Blaha, *Phys. Rev. B* **82**, 205104 (2010).

²⁶J. Sucher, *Phys. Rev. A* **22**, 348 (1980).

²⁷M. H. Mittleman, *Phys. Rev. A* **24**, 1167 (1981).

²⁸A. N. Christensen, *Acta Chem. Scand.* **44**, 851 (1990).

²⁹C. E. Rice and W. R. Robinson, *Mater. Res. Bull.* **11**, 1355 (1976).

³⁰S. A. Howard, J. K. Yau, and H. U. Anderson, *J. Appl. Phys.* **65**, 1492 (1989).

³¹S. Kumarakrishnan, N. L. Peterson, and T. O. Mason, *J. Phys. Chem. Solids* **46**, 1007 (1985).

³²W. R. Robinson, *Acta Crystallogr. Sect. B* **31**, 1153 (1975).

³³K. D. Rogers, *Powder Diffr.* **8**, 240 (1993).

³⁴M. Baster, F. Bourée, A. Kowalska, and Z. Latacz, *J. Alloys Compd.* **296**, 1 (2000).

³⁵J. K. Burdett, G. J. Miller, J. W. Richardson Jr., and J. V. Smith, *J. Am. Chem. Soc.* **110**, 8064 (1988).

³⁶M. Kuriyama and S. Hosoya, *J. Phys. Soc. Jpn.* **17**, 1022 (1962).

³⁷P. Norby, I. G. K. Andersen, E. K. Andersen, and N. H. Andersen, *J. Solid State Chem.* **119**, 191 (1995).

³⁸W. H. Baur, *Acta Crystallogr. Sec. B* **32**, 2200 (1976).

³⁹H. Fjellvåg, F. Grønvold, S. Stølen, and B. Hauback, *J. Solid State Chem.* **124**, 52 (1996).

⁴⁰W. C. Koehler and E. O. Wollan, *J. Phys. Chem. Solids* **2**, 100 (1957).

⁴¹N. C. Tombs and H. P. Rooksby, *Nature (London)* **165**, 442 (1950).

⁴²G. Thornton, B. C. Tofield, and A. W. Hewat, *J. Solid State Chem.* **61**, 301 (1986).

⁴³C. Barrett and E. Evans, *J. Am. Ceram. Soc.* **47**, 533 (1964).

⁴⁴R. D. Shannon, *Acta Crystallogr. Sec. A* **32**, 751 (1976).

⁴⁵H. M. Evjen, *Phys. Rev.* **39**, 675 (1932).

⁴⁶R. S. Mulliken, *J. Chem. Phys.* **23**, 1833 (1955).

⁴⁷G. Radtke, S. Lazar, and G. A. Botton, *Phys. Rev. B* **74**, 155117 (2006).

- ⁴⁸Y. Uehara, D. W. Lindle, T. A. Callcott, L. T. Terminello, F. J. Himpsel, D. L. Ederer, J. H. Underwood, E. M. Gullikson, and R. C. C. Perera, *Appl. Phys. A* **65**, 179 (1997).
- ⁴⁹J.-H. Park, L. H. Tjeng, A. Tanaka, J. W. Allen, C. T. Chen, P. Metcalf, J. M. Honig, F. M. F. de Groot, and G. A. Sawatzky, *Phys. Rev. B* **61**, 11506 (2000).
- ⁵⁰R. Zimmermann, R. Claessen, F. Reinert, P. Steiner, and S. Hüfner, *J. Phys. Condens. Matter* **10**, 5697 (1998).
- ⁵¹Y. S. Dedkov, A. S. Vinogradov, M. Fonin, C. König, D. V. Vyalikh, A. B. Preobrajenski, S. A. Krasnikov, E. Y. Kleimenov, M. A. Nesterov, U. Rüdiger, S. L. Molodtsov, and G. Güntherodt, *Phys. Rev. B* **72**, 060401R (2005).
- ⁵²B. Gilbert, B. H. Frazer, A. Belz, P. G. Conrad, K. H. Nealon, D. Haskel, J. C. Lang, G. Srajer, and G. De Stasio, *J. Phys. Chem. A* **107**, 2839 (2003).
- ⁵³K. Kuepper, M. C. Falub, K. C. Prince, V. R. Galakhov, I. O. Troyanchuk, S. G. Chiuzbaian, M. Matteucci, D. Wett, R. Szargan, N. A. Ovechkina, Y. M. Mukovskii, and M. Neumann, *J. Phys. Chem. B* **109**, 9354 (2005).
- ⁵⁴T. J. Regan, H. Ohldag, C. Stamm, F. Nolting, J. Lüning, J. Stöhr, and R. L. White, *Phys. Rev. B* **64**, 214422 (2001).
- ⁵⁵M. Abbate, F. M. F. de Groot, J. C. Fuggle, A. Fujimori, O. Strebel, F. Lopez, M. Domke, G. Kaindl, G. A. Sawatzky, M. Takano, Y. Takeda, H. Eisaki, and S. Uchida, *Phys. Rev. B* **46**, 4511 (1992).
- ⁵⁶S. C. Wi, J.-S. Kang, J. H. Kim, S. S. Lee, S.-B. Cho, B. J. Kim, S. Yoon, B. J. Suh, S. W. Han, K. H. Kim, K. J. Kim, B. S. Kim, H. J. Song, H. J. Shin, J. H. Shim, and B. I. Min, *Phys. Status Solidi B* **241**, 1529 (2004).
- ⁵⁷M. W. Haverkort, Z. Hu, J. C. Cezar, T. Burnus, H. Hartmann, M. Reuther, C. Zobel, T. Lorenz, A. Tanaka, N. B. Brookes, H. H. Hsieh, H. J. Lin, C. T. Chen, and L. H. Tjeng, *Phys. Rev. Lett.* **97**, 176405 (2006).
- ⁵⁸M. Medarde, C. Dallera, M. Grioni, J. Voigt, A. Podlesnyak, E. Pomjakushina, K. Conder, T. Neisius, O. Tjénberg, and S. N. Barilo, *Phys. Rev. B* **73**, 054424 (2006).
- ⁵⁹G. Vankó, J.-P. Rueff, A. Mattila, Z. Németh, and A. Shukla, *Phys. Rev. B* **73**, 024424 (2006).
- ⁶⁰K. Knížek, Z. Jiráček, J. Hejtmánek, and P. Novák, *J. Phys. Condens. Matter* **18**, 3285 (2006).
- ⁶¹F. M. F. de Groot, J. C. Fuggle, B. T. Thole, and G. A. Sawatzky, *Phys. Rev. B* **41**, 928 (1990).
- ⁶²S. O. Kucheyev, T. van Buuren, T. F. Baumann, J. J. H. Satcher, T. M. Willey, R. W. Meulenberg, T. E. Felter, J. F. Poco, S. A. Gammon, and L. J. Terminello, *Phys. Rev. B* **69**, 245102 (2004).
- ⁶³F. M. F. de Groot, M. O. Figueiredo, M. J. Basto, M. Abbate, H. Petersen, and J. C. Fuggle, *Phys. Chem. Minerals* **19**, 140 (1992).